Advanced Engineering Materials

ADVANCED ENGINEERING MATERIALS
www.aem-journal.com

RESEARCH ARTICLE

Atmospheric AACVD Growth of Nd^{3+}: ZnO Thin Films With Temperature-Optimized Crystallinity and Up-Conversion Quantum Yield

Rida Elleuch[1] | Marwa ben Chobba[2] | Ikram Benammar[2,3] | Jean-Luc Deschanvres[4] | Ramzi Maalej[1] | Abdullah Y. A. Alzahrani[5] | Youssef O. Al-Ghamdi[6] | Sherif M. A. S. Keshk[7]

[1]Laboratoire des Matériaux Composites, Céramiques et Polymères, Faculté des Sciences de Sfax, Université de Sfax, Sfax, Tunisia | [2]Laboratory of Advanced Materials, National School of Engineers of Sfax, University of Sfax, Sfax, Tunisia | [3]Laboratory for Materials and Durability of Constructions, University of Technology of Tarbes, Tarbes, France | [4]Laboratoire des Matériaux et du Génie Physique, Grenoble, France | [5]Department of Chemistry, Faculty of Science, King Khalid University, Abha, Saudi Arabia | [6]Department of Chemistry, College of Science Al-zulfi, Majmaah University, Al-Majmaah, Saudi Arabia | [7]Department Tech and Nanoscience 63 rue de Tolbiac, Paris, France

Correspondence: Marwa ben Chobba (marwa.benchobba@enis.tn)

Received: 8 February 2026 | **Revised:** 29 April 2026 | **Accepted:** 15 May 2026

Keywords: aerosol-assisted chemical vapor deposition | deposition temperature | Nd^{3+}: ZnO thin films | photonic thin films | rare-earth doping | up-conversion luminescence

ABSTRACT

Thin films doped with rare-earth ions often suffer from poor crystallinity and low up-conversion quantum yield (UCQY), limiting their use in photonic and energy-conversion devices. Nd^{3+} ions remain particularly underexplored when doped in thin-film, with no established route for achieving efficient visible up-conversion (UC). Here, we develop an aerosol-assisted chemical vapor deposition (AACVD) process operated at atmospheric pressure to fabricate Nd^{3+} ZnO thin films on Si(111). Systematic variation of the deposition temperature (370–500°C), followed by post-annealing at 1000°C, reveals a direct correlation between Nd incorporation, ZnO crystallinity, and UCQY. Films deposited at 430°C incorporate 2.97 at.% Nd and exhibit optimal *c*-axis orientation and a refractive index of ~2.03. Under 808 nm excitation, these films display strong visible UC emissions at 540, 618, and 680 nm, achieving a total UCQY of 4.25 ± 0.1%. Mechanistic analysis indicates a two-photon process involving excited-state absorption (ESA), energy transfer (ET), cooperative energy transfer (CET), and cross-relaxation (CR), with concentration quenching occurring above ~3 at.% Nd. This study presents a temperature-dependent AACVD method that optimizes Nd incorporation and ZnO microstructure for efficient visible UC. This provides a cost-effective and scalable pathway for high-performance Nd-activated photonic thin films.

1 | Introduction

Up-conversion luminescence is a nonlinear optical process in which two or more low-energy photons are sequentially absorbed and re-emitted as a single higher-energy photon [1]. This behavior originates from the shielded 4f orbitals of rare-earth ions, which enable sharp optical transitions and long-lived excited states [2].

Neodymium (Nd^{3+}) was selected as the dopant because its 4f electronic structure supports efficient two-photon up-conversion pathways, while its ionic radius (0.983 Å, CN = 6) is sufficiently close to that of Zn^{2+} (0.74 Å, CN = 4) to allow partial substitution within the ZnO lattice. This radius compatibility enables Nd^{3+} to occupy Zn^{2+} sites with moderate lattice distortion, promoting defect-mediated absorption and enhancing up-conversion efficiency without destabilizing the wurtzite structure. Because of these properties, up-converting thin films are increasingly important in photonic technologies, including spectral conversion for photovoltaics [3, 4], optical data storage, and visible-light emitters for integrated photonic devices. Among rare-earth ions, Er^{3+}

and Yb^{3+} have been the primary focus of high-efficiency up-conversion systems, with benchmark performances demonstrated in β-$NaYF_4$:Yb^{3+}/Er^{3+} [5] and in optimized Er^{3+}/Yb^{3+} compositions reported by Boyer et al. [6]. These studies established the importance of controlled energy-transfer pathways for achieving high quantum yields. However, they also reveal a critical gap: systematic investigations of other rare-earth ions, particularly Nd^{3+}, remain limited, especially in thin-film form. Thin films typically exhibit lower up-conversion efficiency than powders or bulk materials due to reduced crystallinity, higher defect densities, and enhanced nonradiative quenching [7]. Several deposition routes have been explored for rare-earth-doped thin films, but many face limitations in uniformity, adhesion, or scalability. Wet-chemistry methods such as sol–gel and spin-coating often yield nonuniform films with poor adhesion [8, 9], while pulsed-laser deposition provides high-quality films but remains complex and unsuitable for large-area production [10]. In contrast, aerosol-assisted chemical vapor deposition (AACVD) operates at atmospheric pressure and enables large-area growth with high precursor flexibility and controlled stoichiometry [11]. Its successful application to rare-earth-doped oxides demonstrates the potential of AACVD for producing up-converting thin films [12]. ZnO is a promising host for rare-earth activation due to its wide bandgap, high refractive index, and compatibility with AACVD processing [13]. However, undoped ZnO thin films inherently contain oxygen vacancies, zinc interstitials, and other native point defects that act as deep-level traps and nonradiative recombination centers, limiting their optical efficiency. These defect states broaden emission bands and reduce the likelihood of multiphoton processes. Incorporating neodymium (Nd^{3+}) modifies the defect landscape by partially substituting Zn^{2+} sites, suppressing vacancy-related recombination pathways, and introducing well-defined 4f energy levels that enhance up-conversion efficiency.

Previous studies have shown that Er^{3+}/Yb^{3+}-doped ZnO films can achieve efficient near-infrared-to-visible up-conversion under 980 nm excitation [14], while Nd-based systems have primarily focused on down-conversion or infrared emission [12]. However, no systematic study has established how deposition temperature governs Nd incorporation, ZnO crystallinity, densification, and visible up-conversion efficiency under 808 nm excitation. This gap is significant because Nd^{3+} exhibits strong intra-4f transitions that can yield visible emissions at 540, 618, and 680 nm [15], and ZnO provides a suitable wide-bandgap host for these transitions. In this work, we address this gap by developing an atmospheric-pressure AACVD process that correlates substrate temperature (370°C–500°C) with Nd incorporation, film densification, refractive index, and up-conversion performance. We demonstrate visible up-conversion at 540, 618, and 680 nm from single-ion Nd^{3+}:ZnO thin films, achieving an optimized quantum yield of 4.25 ± 0.1% at 430°C. Mechanistic analysis indicates a two-photon process involving excited-state absorption, energy transfer, cooperative energy transfer, and cross-relaxation, with concentration quenching above ~3 at.% Nd. This process–structure–property mapping establishes AACVD as a scalable and cost-effective route for Nd-activated up-converting thin films for photonic and energy-conversion applications.

2 | Experimental

2.1 | Materials

Zinc acetylacetonate hydrate ($Zn(C_5H_7O_2)_2$, ≥99%, Sigma–Aldrich) and neodymium (III) tris (2,2,6,6-tetramethyl-3,5-heptadionate) (Nd $(TMHD)_3$, ≥99%, STREM Chemicals) were used as the zinc precursor and the dopant source, respectively. Analytical grade methanol and butanol (1:1 v/v, Merck) were used as solvents to prepare a 0.05 M solution with 10 mol.% Nd/Zn. The mixture was magnetically stirred for 1 h at 80°C to ensure homogeneity. Silicon (111) wafers (n-type, thickness ~500 μm) were used as substrates after ultrasonic cleaning using acetone, ethanol, and deionized water, followed by nitrogen drying. All chemicals were used as-received without further purification.

2.1.1 | Thin Film Deposition

Nd-doped ZnO thin films (3 inches × 3 inches) were deposited on Si (111) substrates using a hot-walled AACVD reactor operated at atmospheric pressure, following the procedure described in the literature [16].

The influence of deposition temperature on film structure and luminescence was investigated by varying it in the 370–500°C range. This window was selected to activate $Zn(acac)_2$ and $Nd(TMHD)_3$ while maintaining stable aerosol transport: temperatures below 370°C do not provide sufficient energy for precursor decomposition or ZnO nucleation, whereas temperatures above 500°C cause rapid solvent flash-off and reduced droplet residence time, hindering Nd incorporation and uniform growth. This range is consistent with previous AACVD studies on ZnO and rare-earth-doped ZnO thin films. $Zn(C_5H_7O_2)_2$ and $Nd(TMHD)_3$ were dissolved in a methanol–butanol mixture (1:1 v/v) to prepare a 0.05 M precursor solution with a fixed Nd/Zn molar ratio of 10 mol.%. The solution was magnetically stirred for 1 h at 80°C to ensure complete dissolution. Nd^{3+} doping occurred through substitutional incorporation, where Nd^{3+} ions replace Zn^{2+} sites in the ZnO lattice. The 10 mol.% Nd/Zn precursor ratio yielded approximately 2.9–3.0 at.% Nd in the deposited films. Nd^{3+} is a suitable dopant for ZnO because its ionic radius (0.983 Å) is sufficiently close to that of Zn^{2+} (0.74 Å) to allow partial substitution while inducing controlled lattice distortion. Its lower electronegativity (1.14 vs. 1.65 for Zn) promotes defect modulation, particularly oxygen-vacancy-related states, and its 4f electronic structure provides the intra-4f transitions required for efficient up-conversion. These combined structural, electronic, and defect-level compatibilities make Nd^{3+} an effective dopant for ZnO. During deposition, the precursor solution was placed on an ultrasonic piezoelectric transducer to generate monodisperse droplets (2–4 μm). The aerosol was delivered to the heated substrate at 2 cm^3/min with air flowing at 4 L/min as the carrier gas. Deposition was carried out at substrate temperatures of 643–773 K (370–500°C), ensuring precursor activation while avoiding premature aerosol decomposition. The droplets underwent rapid thermal decomposition upon impingement on the substrate, releasing Zn and Nd species that nucleated and crystallized into the ZnO matrix. Post-deposition annealing was performed in open air at 1000°C for 1 h.

This temperature removes residual organics from AACVD precursors, promotes lattice relaxation, and enhances crystallinity in Nd-doped ZnO, consistent with high-temperature treatments reported for ZnO-based thin films. Thin-film ZnO can withstand annealing above one-third of its bulk melting temperature due to its low thickness and efficient heat dissipation through the Si substrate. Each deposition was sustained for 30 min, producing uniform and adherent thin films.

Aerosol flow, droplet size, and substrate heating were carefully controlled to ensure reproducible morphology, dense coverage, and effective incorporation of Nd^{3+} ions into the ZnO host lattice, demonstrating the advantages of AACVD for large-area thin-film fabrication with precise stoichiometric control.

2.2 | Characterization Methods

The atomic percentages of Nd incorporated into the ZnO films and their densities were determined using electron probe microanalysis (EPMA) [17]. AFM (Veeco Metrology Group Di 3100 NanoScope IIIa) was used to resolve surface morphology and roughness.

Fourier transform infrared spectroscopy (FTIR) detects residual organics and hydroxyl groups, X-ray diffraction (XRD) evaluates phase purity and *c*-axis crystallinity, ellipsometry extracts refractive index and optical density, and PL/UC measurements correlate structural evolution with Nd^{3+} up-conversion efficiency. The influence of up-conversion quantum yield (UCQY) on excitation power density was investigated using neutral density filters, which maintained a consistent beam area throughout the tests. The density values carry an experimental uncertainty of ±2.5%, calculated from three independent measurements, while the Nd doping content determined by EDX exhibits an estimated quantification error of ±0.3 at.% (≈±8%). To guarantee proper photon balance, the integrating sphere was mounted on the fluorometer with entry and output ports arranged at a 90° geometry in the spectrometer plane. The presence of hydroxyl groups and organic residues was investigated using Fourier transform infrared spectroscopy (FTIR, Bio-Rad FTS165), with spectra recorded in the 4000–250 cm^{-1} range at a 4 cm^{-1} resolution under normal incidence. The structural properties were analyzed using X-ray diffraction (XRD, Siemens D8 Advance diffractometer) in a θ–2θ geometry.

The refractive index and thickness were measured using an ellipsometer (Gaertner L116B), with a 632.8 nm exciting wavelength. The photoluminescence (PL) spectra of the Nd^{3+} ions were collected under a 450 nm excitation (12 mW) using an argon laser (Spectra Physics, Model 2017). The emission was analyzed in the 500–750 nm range with a monochromator equipped with a 600 lines/mm grating and a CCD detector (Spectrum One, Jobin Yvon), which provided a 1 nm spectral resolution. The UC spectra were recorded under 808 nm excitation using a Ti:Sapphire ring laser pumped using a CW argon ion laser, with a photomultiplier (Hamamatsu R636) detecting the emission.

The UCQY value was measured using a spectrofluorometer (Edinburgh Instruments FLS920), which was equipped with an integrating sphere (Jobin Yvon) and a liquid-nitrogen-cooled 808 nm laser (Hamamatsu R5587). Circular film samples of 5 mm diameter were positioned at the focal point of the excitation beam.

The relative error in the UCQY measurements was estimated at ~5%. Undoped ZnO films were used as reference samples and mounted in synthetic quartz dishes to suppress background luminescence and eliminate contributions from the ZnO host matrix.

3 | Results and Discussion

The temperature-dependent development behavior of AACVD-derived ZnO:Nd thin films was determined by comprehensively evaluating the structure-property connections influencing Nd incorporation, crystallinity, morphology, optical density, and UC performance. The following subsections provide a sequential investigation of deposition temperature, dopant incorporation, microstructural evolution, optical compactness, and visible UCQY under 808 nm excitation. For each characterization, the behavior of Nd^{3+}:ZnO thin films is explicitly compared with undoped ZnO and with the corresponding annealed samples to highlight dopant-induced structural and optical modifications.

3.1 | Nd^{3+} Incorporation and Film Density

The Nd content exhibited a clear temperature-dependent minimum at 430°C (2.97 at.%). The film density followed the same trend, reaching 5.87 g/cm^3 at 430°C before increasing again at higher temperatures, as shown in Figure 1 and summarized in Table 1.

At elevated temperatures (450–500°C), the decrease in refractive-index-derived density together with the increase in AFM roughness indicates a transition toward less efficient surface growth.

These trends, consistent with AACVD thermal–fluid behavior, arise from rapid solvent flash-off and shortened droplet residence

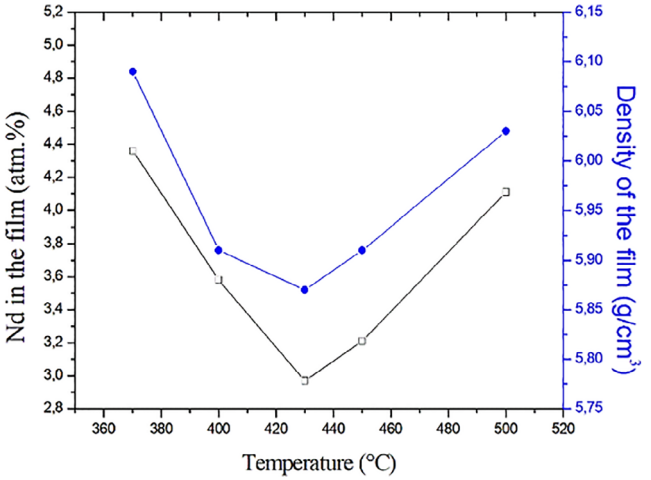

FIGURE 1 | Nd atomic percentages and film densities at different deposition temperatures for the ZnO:Nd thin films deposited at atmospheric pressure using AACVD.

TABLE 1 | Zn, O, and Nd atomic percentages and film density at different deposition temperatures.

Temperature (°C)	Zn (at.%)	O (at.%)	Nd (at.%)	Density (g/cm^3)
370	48.24	49.71	4.36	6.09
400	48.67	49.84	3.58	5.91
430	48.89	49.96	2.97	5.87
450	48.72	49.64	3.21	5.91
500	47.63	47.25	4.11	6.03

times that promote re-evaporation or secondary nucleation [11, 18]. Figure 1 shows the temperature-dependent evolution, while Table 1 provides the corresponding numerical values and uncertainties. Compared to undoped ZnO, Nd^{3+}:ZnO films exhibit a stronger density sensitivity to deposition temperature, confirming that Nd incorporation modifies packing efficiency and defect-mediated densification. After annealing, both undoped and Nd-doped films densify, but the Nd^{3+}:ZnO samples show a more pronounced recovery due to lattice relaxation around substituted Nd^{3+} sites. The co-variation of Nd content and density reveals a balance point at 430°C, where precursor atomization, droplet decomposition, and incorporation kinetics maximize crystalline packing while minimizing defect-mediated Nd trapping. This interpretation is supported by AFM, XRD, refractive-index-derived density, and EDX trends (Sections 3.2, 3.3), all of which identify 430°C as the temperature that optimizes densification and controlled Nd incorporation. Below 400°C, incomplete precursor decomposition increases apparent Nd content but reduces densification. At 450°C–500°C, rapid solvent flash-off creates "limited growth zones" that shorten droplet residence time, increasing Nd incorporation but lowering packing efficiency relative to 430°C. The 430°C incorporation window provides the structural basis for the highest UCQY (Section 3.7), where optimized densification and Nd–Nd spacing suppress nonradiative quenching.

In contrast to earlier AACVD studies on Er/Yb-co-doped ZnO that optimized 980 nm up-conversion without mapping single-ion incorporation [12], and ZnO:Nd nanodisks where growth rate dominated optical behavior [19], this work introduces a dual-axis mapping approach. For the first time in Nd:ZnO thin films, a reproducible correlation between deposition temperature, Nd incorporation, and film density is established under atmospheric-pressure AACVD. As shown in Table 1, Zn and O atomic percentages remain close to stoichiometric ZnO but exhibit systematic temperature-dependent deviations that reflect the underlying deposition regime. At 370°C–400°C, a slight Zn/O imbalance indicates incomplete decomposition and hydroxyl-rich intermediates, producing flat, featureless morphologies typical of a surface-reaction-limited regime [20, 21]. At 430°C, Zn and O approach near-ideal stoichiometry, marking the transition to a fully activated decomposition regime with compact, crystalline, adherent films [21]. At 450°C–500°C, reduced O content and slight Zn deficiency signal oxygen-poor growth caused by rapid solvent flash-off, promoting vacancy-assisted Nd incorporation but reducing crystallographic ordering [22, 23]. These stoichiometric trends confirm 430°C as the optimal balance between precursor activation, ZnO lattice formation, and controlled Nd substitution. Mechanistically, the minimum Nd at.% and maximum densification at 430°C correspond to (i) stable 2–4 μm droplet atomization, (ii) solvent evaporation matched to surface reaction rate, and (iii) substitutional Nd^{3+} incorporation without phase separation. This regime is essential for suppressing concentration quenching in a single-dopant Nd^{3+} system while sustaining ESA/CET pathways responsible for two-photon UC. The identified temperature window enhances scalability and photonic applicability beyond previous reports. Sections 3.9, 3.10 further correlate Nd concentration with structural and optical properties and detail the underlying physical mechanisms.

3.2 | Surface Morphology Evolution With Deposition Temperature

The deposited layers are confirmed to be in the thin-film domain by the film thickness, which is in the 200–320 nm range based on AFM step-height and ellipsometry modeling. The surface morphology of the ZnO:Nd thin films deposited using AACVD was then examined as a function of substrate temperature (370–500°C) using AFM. The AFM micrographs for the films deposited at 370, 430, and 500°C reveal a clear transition in surface topography (Figure 2).

As shown in Figure 2a, the film appeared flat and featureless at 370°C, indicating incomplete decomposition of the Zn and Nd precursors. A similar morphology was observed at 400°C, suggesting early-stage nucleation with poorly defined nanograins.

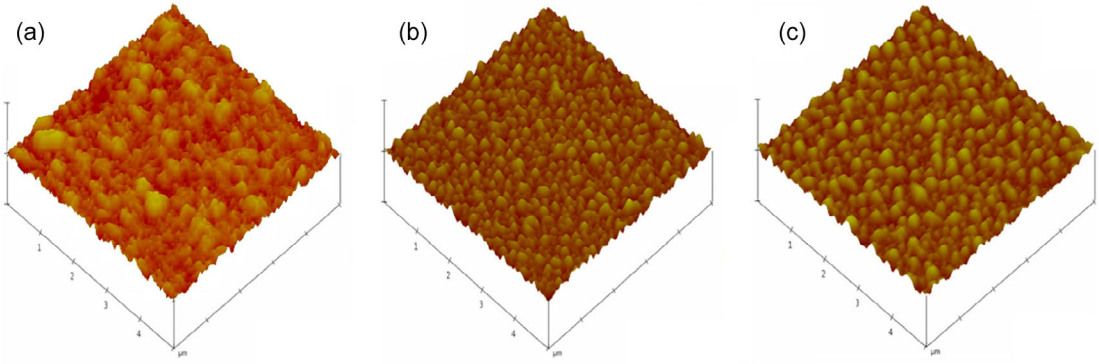

FIGURE 2 | AFM micrographs of the ZnO: Nd thin films deposited at (a) 370, (b) 430, and (c) 500°C using AACVD at atmospheric pressure.

At 430°C, the surface exhibited well-defined nanocrystals with lateral dimensions of 60–70 nm and heights of 160–190 nm, which corresponded to a roughness of ~60 nm (Figure 2b). This temperature marked the onset of complete precursor decomposition, which was facilitated by the low dissociation enthalpy of the Zn and Nd complexes and enabled rapid droplet breakdown and uniform grain formation. The grain size increased slightly (from 60–70 nm to 65–75 nm) as the temperature increased to 500°C. (Figure 2b), but the surface became more densely packed and crystallographically ordered. These qualitative AFM observations are quantitatively supported by the grain-size and roughness values summarized in Table 2, which clearly reflect the temperature-dependent evolution of nucleation, grain coalescence, and surface development in AACVD-grown ZnO:Nd films.

For the as-deposited samples, the grain size increases from 40–50 nm at 400°C to 60–70 nm at 430–450°C and further to 65–75 nm at 500°C, while the roughness stabilizes around ~60 nm. This result confirms the switch from a poorly nucleated, reaction-limited environment at low temperatures to a fully established columnar growth regime once precursor breakdown is completed at 430°C [24–26]. At ≥450°C, the roughness remains nearly constant despite increasing grain size, indicating a diffusion-limited regime in which rapid solvent flash-off suppresses vertical growth and favors lateral grain coalescence. Annealing at 1000°C results in obvious grain coarsening (75–85 nm for the 430°C film) and increased roughness (up to ~80 nm), indicating thermally induced grain development and improved crystallite connectivity. The film deposited at 430°C has the highest post-annealing grain size and roughness, indicating excellent initial crystallinity and densification. This response confirms that the microstructure created at 430°C provides the best template for subsequent thermal refinement, allowing for more efficient grain boundary migration and lattice ordering during annealing. Table 2 shows a strong correlation between deposition temperature, as-deposited morphology, and annealing-induced grain evolution, confirming 430°C as the best growth temperature for Nd^{3+}:ZnO thin films. Compared to undoped ZnO, Nd-doped films show more pronounced grain development and roughness sensitivity, indicating that Nd incorporation enhances nucleation kinetics and modifies surface-energy-driven growth. At higher temperatures, the formation of 'limited growth zones' slightly increases roughness (68–72 nm), consistent with restricted droplet dissociation and surface saturation under AACVD conditions [18]. This temperature-dependent morphological evolution confirms the transition from reaction-limited to diffusion-limited growth, in agreement with the AACVD growth regimes described by Hou and Choy [11]. Although temperature-induced densification in ZnO:Er films was previously reported [18], systematic mapping of roughness evolution and its correlation with UC-active dopant incorporation was not addressed. The present work establishes, for the first time, a direct correlation between deposition temperature, surface morphology, and Nd^{3+} incorporation in AACVD-grown ZnO thin films. The emergence of well-defined grains at 430°C coincides with optimal densification and controlled Nd incorporation, providing the structural basis for the enhanced UCQY observed. This dual optimization of morphology and dopant distribution distinguishes the present approach from earlier studies on Er/Yb-co-doped ZnO [12] and Nd:Y_2O_3 coatings [27], which lacked systematic mapping of surface states.

3.3 | Structural and Chemical Integrity of Nd^{3+}: ZnO Thin Films

The structural evolution of the ZnO:Nd thin films deposited using AACVD was investigated via XRD and FTIR spectroscopy. The XRD patterns of the films deposited at 370°C–500°C and the one annealed at 1000°C are presented in Figure 3. All samples exhibited diffraction peaks corresponding to the hexagonal wurtzite ZnO phase, with dominant reflections indexed to the (002), (101), (102), (103), and (112) planes. The absence of secondary phases, such as Nd_2O_3, confirmed the successful incorporation of the Nd^{3+} ions into the ZnO lattice without phase segregation, which was consistent with the prior reports on Nd-doped ZnO systems [28]. The film deposited at 430°C had the most intense and sharp (002) peak, indicating optimal crystallinity and a preferred *c*-axis orientation. Furthermore, this orientation reflected vertical columnar growth along the lowest surface energy plane of the ZnO hexagonal structure, which was typical of the AACVD-grown films [17, 18]. The enhanced crystallinity observed at 430°C correlated directly with the optimum densification and Nd incorporation, providing a robust structural basis for improved UCQY.

The film deposited at 430°C had the most intense and sharp (002) peak, indicating optimal crystallinity and a preferred *c*-axis orientation. Furthermore, this orientation reflected vertical columnar growth along the lowest surface energy plane of the ZnO hexagonal structure, which was typical of the AACVD-grown films [17, 18]. The enhanced crystallinity observed at 430°C correlated directly with the optimum densification and Nd incorporation, providing a robust structural basis for improved UCQY. The subsequent annealing at 1000°C further sharpened the diffraction peaks, which indicated grain growth and improved lattice

TABLE 2 | Grain size (nm) and roughness (nm) of the deposited and annealed ZnO:Nd films at 1000°C.

	Deposited films		Annealed films at 1000°C	
Deposition temperature (°C)	**Grain size (nm)**	**Roughness (nm)**	**Grain size (nm)**	**Roughness (nm)**
370	—	—	30–40	30
400	40–50	40	45–55	50
430	60–70	60	75–85	80
450	60–70	60	65–75	70
500	65–75	60	65–75	70

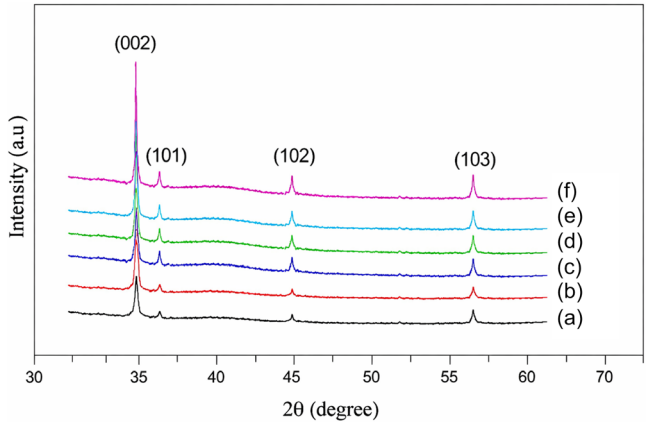

FIGURE 3 | XRD patterns of the ZnO:Nd thin films deposited using AACVD at atmospheric pressure at (a) 370°C, (b) 400°C, (c) 430°C, (d) 450°C, (e) 500°C, and (f) annealed at 1000°C.

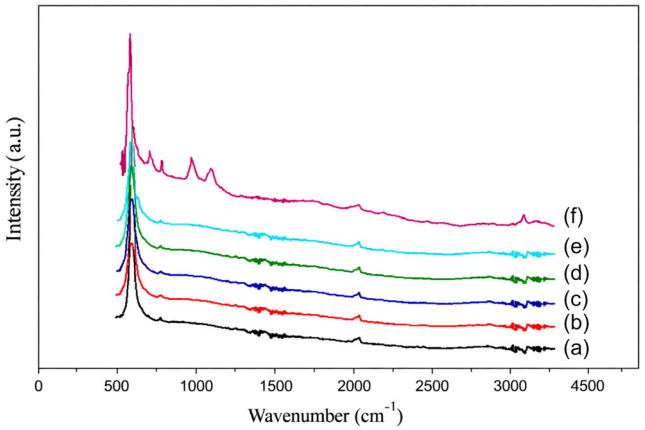

FIGURE 4 | FTIR spectra of the ZnO: Nd thin films deposited using AACVD at atmospheric pressure at (a) 370°C, (b) 400°C, (c) 430°C, (d) 450°C, (e) 500°C, and (f) annealed at 1000°C.

ordering. Importantly, the absence of the secondary phases confirmed the thermal stability of the Nd^{3+}-substituted ZnO matrix. This behavior was in contrast with the Nd:Y_2O_3 coatings, where annealing frequently induced phase separation or Nd clustering [12]. Table 3 summarizes the temperature-dependent evolution of the (002) peak position, d spacing, and crystallite size, demonstrating Nd incorporation into the ZnO lattice.

The ICDD reference (01-089-0510) identifies the bulk ZnO (002) peak at 34.44° ($d = 2.603$ Å). In Nd-doped films, the peak shifts to lower angles as Nd content increases, for example, 34.21° at 4.36 at.% Nd (370°C) and 34.18° at 4.11 at.% Nd (500°C), representing *c*-axis expansion induced by substitution of the bigger Nd^{3+} ion (0.98 Å) for Zn^{2+} (0.74 Å) [29–31]. At 430°C, when Nd incorporation is lowest (2.97 at.%), the (002) peak shifts closer to the bulk value (34.26°, $d = 2.614$ Å), showing minimum lattice distortion and regulated substitution. These patterns suggest that Nd incorporation is the principal source of lattice strain, and that 430°C gives the most coherent and least-distorted Nd:ZnO lattice, corresponding with the improved UCQY at this temperature.

Compared to undoped ZnO, Nd^{3+}:ZnO films exhibit a consistent (002) shift to lower angles, indicating substitutional Nd incorporation. After annealing at 1000°C, both undoped and Nd-doped films show sharper peaks. However, the Nd-doped films had a bigger *c*-axis expansion, indicating stable Nd incorporation without phase segregation. The FTIR spectra of the same films are shown in Figure 4. The characteristic Zn–O stretching vibration at ~410 cm^{-1} confirmed the presence of the wurtzite ZnO phase.

TABLE 3 | Shifting angle of (002) *c*-axis, d spacing, and crystallite size according to the deposition temperatures.

Deposition temperature (°C)	Nd (at.%)	2θ (°)	d (Å)	Crystallite size (nm)
370	4.36	34,21	2622	20.927
400	3.58	34,23	2617	18.886
430	2.97	34,26	2614	17.356
450	3.21	34,24	2615	18.112
500	4.11	34,18	2,62	20.108

The organic residue bands between 1300 and 1700 cm^{-1} were attributed to the residual carbonyl and alkene groups (ν[C═C], ν[C═O], and γCH_3), which originated from the incomplete precursor decomposition [32]. The bands at 1556–1571 cm^{-1} corresponded to the C═C or C═O stretching vibrations, while the broad absorptions in the 3500–4000 cm^{-1} range were assigned to the –OH stretching modes, indicating surface hydroxylation and adsorbed moisture [18]. Post-annealing spectra showed reduced intensity of the organic bands and sharper Zn–O features, confirming thermal removal of the residual organics and enhanced lattice purity [33].

The presence of residual hydroxyl and weak carbonate/moisture-related bands indicates that the films are not fully dehydroxylated, reflecting incomplete precursor decomposition and post-deposition surface hydroxylation typical of AACVD-grown oxide films. The combined XRD-FTIR technique used in this investigation gave a more thorough image of phase purity and chemical integrity than prior AACVD studies for the ZnO:Er and ZnO:Yb systems, which lacked detailed FTIR analysis [34]. This dual validation supported the claim that Nd^{3+} ions were substituted into ZnO without creating secondary phases. The 430°C deposition temperature resulted in structurally and chemically optimized films for up/down conversion applications. Undoped ZnO has stronger OH- and carbon-related absorption bands, whereas Nd^{3+}:ZnO films exhibit significantly lower intensities, especially after annealing. Annealed Nd-doped films have the most distinct Zn-O vibrational mode, indicating effective elimination of organic residues and enhanced lattice ordering. Compared to undoped ZnO, Nd^{3+}After annealing, ZnO films show much decreased hydroxyl-related absorbance, indicating dopant-assisted densification and efficient removal of residual organics.

3.4 | Thermal Annealing Effects on Phase Purity and Crystallinity

The use of β-di-ketonate precursors in the liquid AACVD process often results in ZnO:Nd films containing residual hydroxyl groups and organic contaminants, which are known to introduce nonradiative recombination pathways to quench RE luminescence [16].

Consequently, to mitigate these residual defects, thermal annealing in air at 1000°C was applied to the film deposited at 430°C, which was the optimal condition identified for Nd^{3+} incorporation and densification. The XRD patterns before and after annealing are shown in Figure 3. The annealed film exhibited sharper and more intense diffraction peaks, particularly along the (002) and (101) planes, which indicated improved crystallinity and grain growth [35, 36]. Importantly, the absence of the Nd_2O_3 secondary phase confirmed that the Nd^{3+} ions remained substitutionally incorporated within the ZnO lattice even after a high-temperature treatment [37, 38]. This thermal stability was in contrast with the Nd:Y_2O_3 coatings, where annealing often induced phase segregation [12]. Additionally, this validated the robustness of the AACVD-grown ZnO:Nd matrix of this study. The FTIR analysis further supported the enhancement in crystallinity. Figure 4 shows the FTIR spectrum of an annealed film. The absence of the wide –OH and organic bands (1300–1700 cm^{-1} and 3500–4000 cm^{-1}) indicates the elimination of remaining ligands and adsorbed moisture [25].

Two distinct bands at 912 and 1077 cm^{-1} were attributed to Si—O stretching vibrations, indicating the creation of a thin interfacial SiO_2 layer between the ZnO film and the Si substrate during annealing. This behavior has previously been described in Nd-doped ZnO systems. Annealing at 1000°C results in partial oxidation of the Si substrate, indicating high-temperature Si—O interfacial interactions [28]. Moreover, the increased intensity of the Zn–O vibration at 410 cm^{-1} reflected improved lattice ordering and stronger Zn—O bonding, which was consistent with the sharper XRD peaks. This structural refinement directly supported the enhanced UCQY observed after annealing since the reduced defect density and the formation of cleaner interfaces minimized the nonradiative losses. In contrast to the previous AACVD studies on ZnO:Er and ZnO:Yb films, which lacked post-deposition purification strategies, the approach of this study demonstrated that annealing improved crystallinity and chemically purified the film to enable efficient Nd^{3+} luminescence [12, 18]. This dual structural and chemical optimization reinforces the novelty of the process developed in this study and its suitability for scalable photonic applications. A mechanistic interpretation of these temperature- and doping-dependent changes is provided in Section 3.10.

3.5 | Refractive Index and Porosity

The refractive index and porosity of the ZnO:Nd thin films annealed at 1000°C were extracted using spectroscopic ellipsometry and plotted in Figure 5.

The porosity of the films was described using the Lorentz–Lorenz law and was determined using the following relation

$$P = 1 - \frac{(n^2 - 1)}{(n_s^2 - 1)} \times 100 \quad (1)$$

where n_s (=2.008) and n refer to the refractive index of the annealed ZnO:Nd film, respectively.

These parameters reflected the optical density and microstructural compactness of the film, both of which were critical for the UC

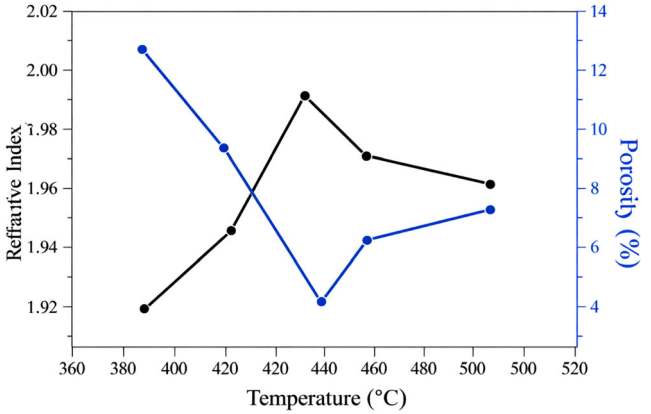

FIGURE 5 | The refractive index and porosity at different deposition temperatures for the ZnO:Nd films annealed at 1000°C.

efficiency and the RE ion activation. For the as-deposited ZnO:Nd films, the refractive index (n) lies in the 1.81–1.83 range and increases upon annealing to reach ~1.99 at 1000°C. As shown in Figure 5, n rises with deposition temperature and peaks at 430°C ($n \approx 1.99$), while the porosity simultaneously reaches a minimum of 2.37%. The refractive-index value ($n \approx 2$) corresponds to the ZnO:Nd layer extracted from thin-film optical modeling, in which the Si substrate ($n \approx 3.4$) is treated as a fixed optical boundary and does not influence the fitted film index. Nd^{3+}:ZnO films exhibit a stronger refractive-index sensitivity to temperature than undoped ZnO, reflecting dopant-induced modifications in packing density and microstructure. Annealing increases the refractive index in both undoped and Nd-doped films, but the enhancement is more pronounced in the Nd-doped samples due to improved lattice ordering around Nd^{3+} sites. The inverse relationship between n and porosity confirms densification and a reduced void fraction, consistent with AFM-observed grain coalescence, XRD-revealed crystallinity enhancement, and FTIR-verified removal of organic residues. The refractive-index maximum at 430°C aligns with the optimum Nd incorporation and film density, indicating that post-annealing interfacial rearrangements may slightly shift the optical peak. The porosity minimum reflects improved packing and fewer scattering centers, directly contributing to the enhanced UCQY. The optical compactness achieved here surpasses previous AACVD reports on ZnO:Er and ZnO:Yb films, which typically showed $n < 1.95$ due to incomplete densification [12, 18]. Likewise, the porosity control exceeds that of Nd:Y_2O_3 coatings, which often suffer from phase separation and poor packing [12]. The refractive-index values obtained are comparable to those of high-quality ZnO:Nd films produced by PLD and sol–gel methods [28], but with the added advantage of atmospheric-pressure AACVD scalability.

This confirms that the annealing strategy used in this work chemically purifies the films and enhances their optical and structural integrity, reinforcing the multifunctional optimization achieved across compositional, morphological, and crystallographic parameters.

3.6 | Room-Temperature PL Emission

The room-temperature PL spectra of the ZnO:Nd thin films annealed at 1000°C under a 450 nm excitation are presented

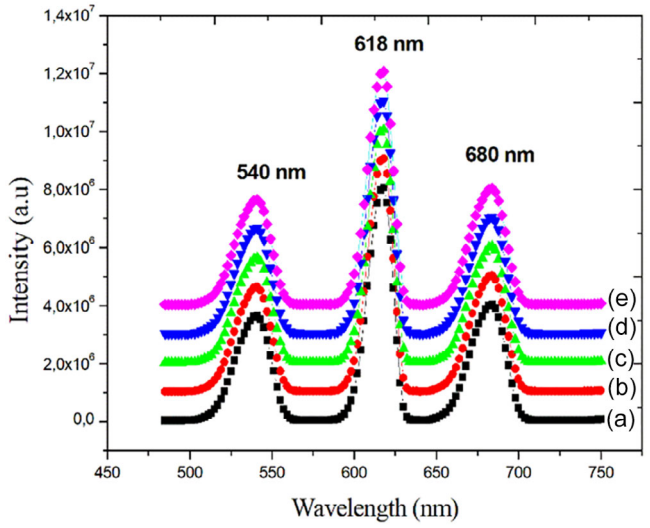

FIGURE 6 | Room-temperature PL emission spectra under 450 nm excitation for the ZnO:Nd films annealed at 1000°C and deposited at (a) 370, (b) 400, (c) 430, (d) 450, and (e) 500°C.

in Figure 6. Additionally, the three distinct emission bands observed at 540, 618, and 680 nm corresponded to the following intra-4f transitions of the Nd^{3+} ions:

- **At 540 nm**: the weak green emission attributed to the $^4G_{7/2} \rightarrow {}^4I_{9/2}$ transition.
- **At 618 nm**: the dominant red emission from the overlapping $^4G_{7/2} \rightarrow {}^4I_{11/2}$ and $^4G_{5/2} \rightarrow {}^4I_{9/2}$ transitions.
- **At 680 nm**: the weak deep-red emission from the $^4G_{7/2} \rightarrow {}^4I_{13/2}$ and $^4G_{5/2} \rightarrow {}^4I_{11/2}$ transitions.

The strongest red emission at 618 nm was observed for the film deposited at 430°C and subsequently annealed at 1000°C, which corresponded to a 2.97 at.% Nd concentration. This emission peak coincided with the optimum densification and crystallinity conditions, where Nd^{3+} ions were uniformly incorporated into the ZnO lattice without phase segregation, and the organic quenching centers were effectively removed, as evidenced by the XRD and FTIR analysis, respectively.

The PL intensity trend across the deposition temperatures confirmed that the film deposited at 430°C offered the most efficient Nd^{3+} activation. This was attributed to optimal Nd–Nd spacing and reduced defect density, which suppressed the nonradiative CR and enhanced the radiative recombination. The correlation between PL intensity and refractive index further supported this observation, with the highest refractive index at 430°C reflecting maximal optical density and minimal porosity, both of which favored photon confinement and emission enhancement. This study demonstrated a single-ion optimization strategy for Nd^{3+} in ZnO compared to the previous studies on the Nd:Y_2O_3 and ZnO:Er/Yb systems, which lacked PL mapping across temperature or relied on cooperative sensitization [12, 27]. The ability to tune PL intensity via deposition temperature and annealing, without requiring co-dopants, represented a novel approach in the AACVD-grown UC materials.

In summary, the intense 618 nm emission validated the structural and chemical optimization achieved at 430°C, and confirms that the Nd^{3+} ions were incorporated and optically active. This emission band served as a spectral fingerprint of the successful doping, enhanced crystallinity, and effective defect suppression to reinforce the multifunctional control achieved across the compositional, morphological, structural, and optical parameters.

3.7 | Room-Temperature UC Emission and Mechanistic Pathways

The room-temperature UC spectrum of the ZnO: Nd thin films annealed at 1000°C and excited at 808 nm is presented in Figure 7a.

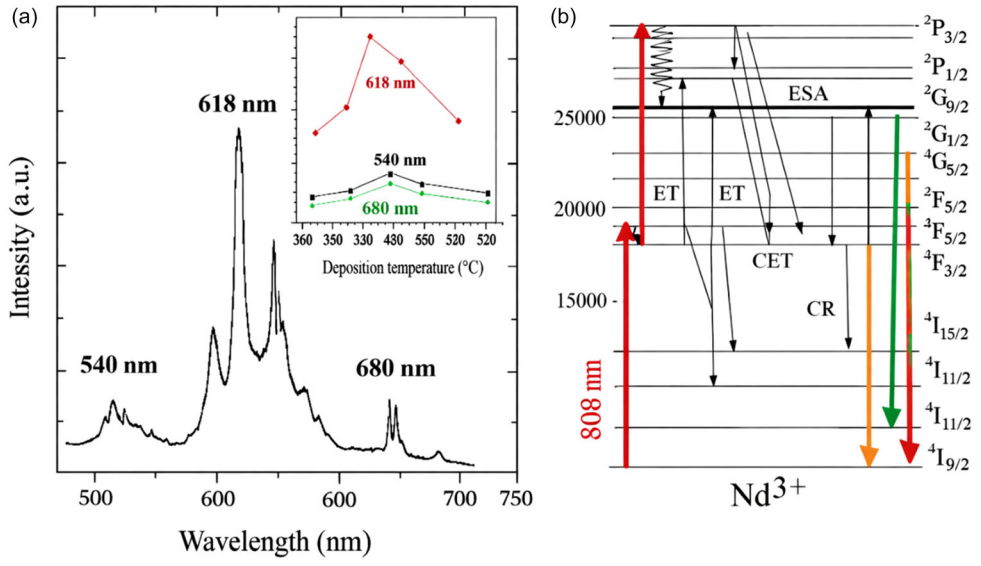

FIGURE 7 | (a) Room-temperature UC emissions of the ZnO:Nd thin films (2.97 at.%) annealed at 1000°C under 808 nm excitation. (b) Energy level diagram of Nd^{3+} ions in ZnO showing UC pathways under 808 nm excitation.

The three prominent emission bands centered at 540, 618, and 680 nm corresponded to the following intra-4f radiative transitions of Nd^{3+} ions: $^4G_{7/2} \rightarrow {}^4I_{9/2}$ at 540 nm, $^4G_{7/2} \rightarrow {}^4I_{11/2}$ and $^4G_{5/2} \rightarrow {}^4I_{9/2}$ at 618 nm, and $^4G_{7/2} \rightarrow {}^4I_{13/2}$ and $^4G_{5/2} \rightarrow {}^4I_{11/2}$ at 680 nm. The film containing 2.97 at.% of Nd showed the most intense emission at 618 nm, confirming that this doping level yielded optimal Nd^{3+} activation. This correlated directly with the densification and crystallinity of the peak at 430°C, the refractive index maximum, and the enhanced PL intensity, which highlighted the convergence of the structural, optical, and emission properties at this deposition condition. As shown in Figure 7b, the energy level diagram of the Nd^{3+} ions in ZnO highlights the mechanistic pathways responsible for the UC emission under 808 nm excitation. The UC process involved the following four key mechanisms:

- **Ground State Absorption (GSA)**: Excitation from the $^4I_{9/2}$ state to the metastable $^4F_{5/2}$.
- **ESA**: Sequential absorption promoting electrons from $^4F_{3/2}$ to higher levels like $^2D_{5/2}$.
- **ET**: Between two Nd^{3+} ions in $^4F_{3/2}$, enabling transitions such as ($^4F_{3/2}$, $^4F_{3/2}$) → ($^4I_{13/2}$, $^4G_{7/2}$).
- **CET** and **CR**: Resonant interactions between ions in excited states, which populate higher levels like $^4G_{11/2}$ and $^4G_{9/2}$ and enhance red emission.

The dominant red emission at 618 nm was attributed to the direct transitions from $^4G_{7/2}$ and to the overlapping emissions from the thermally populated $^4G_{11/2}$ and $^2G_{9/2}$ levels. These were fed via CET and ET processes, as supported by the matched energy gaps and resonant transfer channels [19, 27]. Beyond 2.907 at. %Nd, the UC intensity decreased due to concentration quenching, which was primarily driven by the CR processes. These involved energy loss through the likes of the following nonradiative channels:

($^4G_{7/2}$, $^4I_{9/2}$) → ($^4F_{7/2}$, $^4I_{15/2}$)

($^2G_{7/2}$, $^4I_{9/2}$) → ($^4F_{3/2}$, $^4I_{15/2}$)

Additional CR channels: ($^2G_{11/2}$, $^4I_{9/2}$) → ($^4F_{9/2}$, $^4I_{15/2}$), ($^2G_{9/2}$, $^4I_{9/2}$) → ($^2H_{11/2}$, $^4I_{15/2}$), and ($^2P_{1/2}$, $^4I_{9/2}$) → (2 × $^4F_{3/2}$),

The up-conversion pathways identified here mirror those reported in Ho^{3+}-doped glasses [27], where CR-induced lattice vibrations suppress UC efficiency. In contrast, the present work establishes a single-ion-optimized UC strategy for Nd^{3+}:ZnO, outperforming earlier Nd:Y_2O_3 and ZnO:Er/Yb systems that relied on cooperative sensitization or lacked mechanistic mapping [19, 27]. The controlled Nd–Nd spacing, high phase purity, and precise refractive-index tuning achieved through AACVD enable reproducible and intense visible up-conversion without the need for co-dopants or external sensitizers. Undoped ZnO exhibits only defect-related PL, whereas Nd^{3+}:ZnO films uniquely display strong UC emission at 540, 618, and 680 nm under 808 nm excitation. Annealing enhances PL intensity in both undoped and Nd-doped films; however, only the Nd^{3+}:ZnO samples show a significant UCQY improvement, driven by optimized Nd–Nd spacing, reduced nonradiative quenching, and improved lattice coherence. This confirms that the structural and optical optimization achieved at 430°C directly governs the efficiency of the two-photon ESA/ET/CET-assisted UC process.

3.8 | UCQY and Power Dependence

The UCQY of the NIR-to-visible process was measured under 808 nm excitation to evaluate the UC efficiency of the ZnO:Nd thin films. The UCQY value was calculated using the standard comparative method, where the integrated visible emission ($E_{emission}$) was normalized against the absorbed excitation energy that was determined from the difference between the laser peak of the sample (E_{sample}) and that of an undoped ZnO reference (E_{ref}). Theoretically, the UCQY value for a two-photon process is limited to 50% since two absorbed photons are required per emitted photon. The variation in UCQY with the excitation power density for the ZnO:Nd films annealed at 1000°C is presented in Figure 8a.

The as-deposited films exhibited low UCQY values (~0.9%–1.1%), while the annealed films had significantly enhanced yields in the 2.37%−4.25% range, which confirmed the critical role of the thermal treatment in activating Nd^{3+} ions and removing quenching centers (Sections 3.3 and 3.4). The UC emission intensity showed the saturation threshold at 19.7 ± 0.2 W/cm^2, which was slightly lower than that reported for the β-$NaYF_4$:Er, Yb nanoparticles (20 ± 0.3 W/cm^2), which indicated a more efficient photon utilization in the ZnO:Nd system of this study [17]. The film deposited at 430°C and annealed at 1000°C achieved the highest UCQY of 4.25 ± 0.2%, correlating with the optimal crystallinity (Section 3.3), densification (Section 3.2), and refractive index peak (Section 3.5).

This value surpassed the UCQY values of the colloidal β-$NaYF_4$: Er, Yb nanoparticles (0.3 ± 0.3%) and bulk β-$NaYF_4$ (3.0 ± 0.1%) under similar excitation conditions to position the films of this study as promising candidates for photonic applications, such as bioimaging, photovoltaics, and optical sensing [17]. Additionally, the UCQY values showed a strong dependence on Nd^{3+} concentration, as summarized in Table 4. The maximum total UCQY of 4.25 ± 0.01% was obtained at 2.97 at.% Nd, with individual contributions of 1.21% (540 nm), 1.78% (618 nm), and 1.26% (680 nm). UCQY decreased beyond this concentration due to concentration quenching, which was consistent with the CR pathways that dominated at higher Nd^{3+} loadings.

The double logarithmic plot of UC emission intensity (I) versus excitation power (P) for the 2.97 at.% Nd film is shown in Figure 8b. The slopes (n-values) were 1.92 ± 0.3 (540 nm), 2.08 ± 0.2 (618 nm), and 1.94 ± 0.2 (680 nm), which confirmed that a two-photon absorption mechanism governed the UC process [27]. These values were consistent across all annealed films, reinforcing the reproducibility of the UC behavior. The saturation behavior of the UC intensity with increasing pump power, particularly for the red and deep-red emissions, is further illustrated in Figure 8c. This saturation indicated population bottlenecks and supported the need for optimized doping and excitation regimes. The findings of this study agreed with the previous reports on the Er, Yb co-doped ZnO thin films, where high-temperature annealing was shown to eliminate defect states

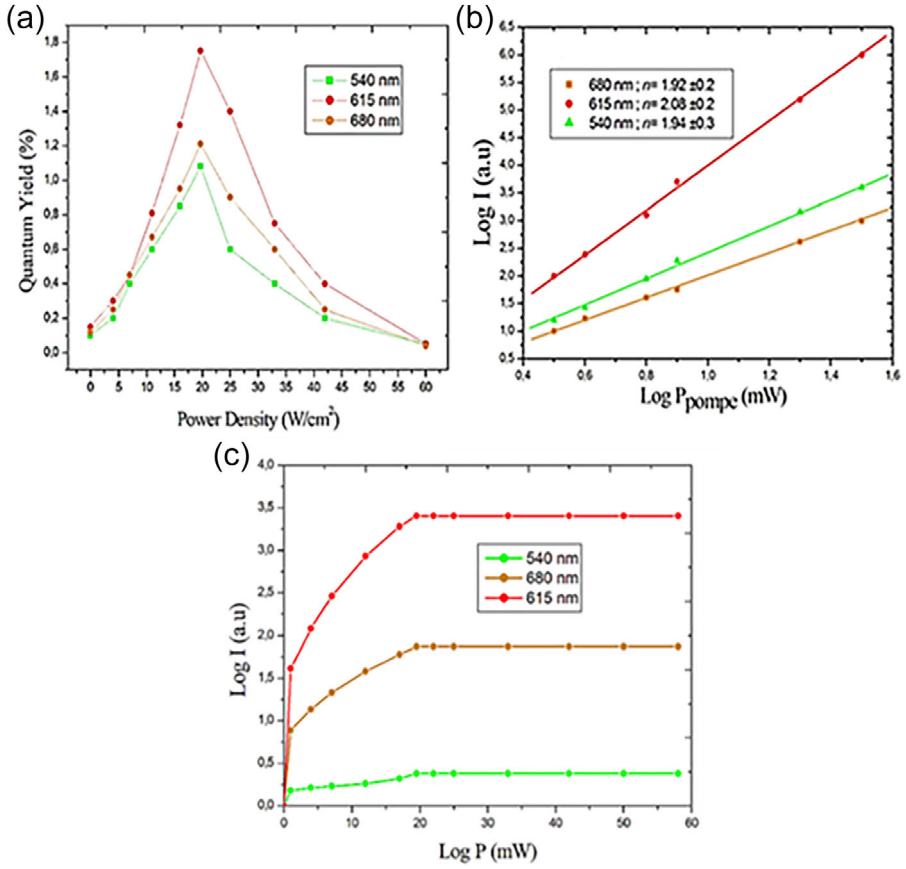

FIGURE 8 | (a) The UCQY variation (in %) for different excitation power densities, (b) log–log plot of UC intensity for excitation powers, and (c) the saturation behavior of the UC intensity for the ZnO:Nd (2.97 at.%) thin film.

TABLE 4 | UCQY values for the ZnO:Nd thin films at different Nd concentrations.

Nd (at.%)	540 nm	618 nm	680 nm	Total UCQY (%)
4.36	0.73 ± 0.01%	0.98 ± 0.01%	0.66 ± 0.02%	2.37 ± 0.01%
3.58	0.96 ± 0.02%	1.11 ± 0.02%	0.88 ± 0.02%	2.95 ± 0.01%
2.97	1.21 ± 0.01%	1.78 ± 0.02%	1.26 ± 0.02%	4.25 ± 0.01%
3.21	1.11 ± 0.02%	1.64 ± 0.01%	0.99 ± 0.01%	3.74 ± 0.01%
4.11	1.05 ± 0.02%	1.58 ± 0.01%	0.82 ± 0.02%	3.45 ± 0.02%

and enhance UC efficiency. Yb^{3+}/Er^{3+} co-doped β-$NaYF_4$ [18] and phosphate glasses [39] have shown similar trends, but without the single-ion optimization demonstrated in this study. In summary, the ZnO: Nd thin films exhibited robust UCQY performance, which could be tuned through the deposition temperature, annealing, and Nd^{3+} concentration.

Therefore, the combination of a high UCQY, low saturation threshold, and reproducible two-photon behavior established a novel and scalable platform for RE ion-based UC materials.

3.9 | Impact of Nd^{3+} Doping on Structural, Morphological, and Optical Properties

Although the deposition temperature affects the breakdown regime and densification behavior, the Nd^{3+} concentration has a critical impact on the structural and optical responses of the films. The Nd concentration ranges from 2.97 to 4.36 at.% between 370 and 500°C, and this variation has a direct impact on grain coalescence, defect density, and optical compactness.

Roughness: Higher Nd loadings (≥4 at.%) are associated with increased surface disorder and failed grain fusion, while 2.97 at. The % regime at 430°C produces the most homogeneous nanocrystals with minimal defect-mediated roughness.

Crystallinity: The strongest (002) orientation corresponds to the lowest Nd concentration, suggesting that excessive Nd^{3+} breaks ZnO lattice ordering, whereas moderate substitution stabilizes *c*-axis growth.

Porosity and Refractive Index: At 2.97 at.% Nd, there is a minimum porosity (2.37%) and a maximum refractive index

($n = 1.99$), indicating that optimal doping increases packing density and decreases scattering centers.

Optical Performance: At the same Nd concentration, the UCQY maximum (4.25 ± 0.1%) is obtained, highlighting the importance of regulated Nd–Nd spacing in preventing concentration quenching and maintaining efficient ESA/ET/CET pathways.

This integrated analysis confirms that Nd^{3+} doping is not only a compositional variable but a fundamental predictor of morphology, crystallinity, optical density, and UC efficiency. Its effect is maximal inside the thermally chosen incorporation window at 430°C.

3.10 | Physical Mechanisms for Doping and Temperature-Induced Variations

Variations in structural and optical characteristics result from the interaction of Nd^{3+} incorporation, precursor decomposition kinetics, and thermally driven defect evolution. At low temperatures (370–400°C), inadequate breakdown of Zn and Nd β-di-ketonates results in hydroxyl-rich, defect-dominated films with limited grain development, leading to greater roughness, porosity, and lower refractive index. At 430°C, the decomposition rate is fully surface reaction-limited, allowing for uniform nucleation, regulated Nd substitution at Zn^{2+} sites, and reduced defect density. This approach improves crystallinity, refractive index, and UCQY simultaneously by minimizing Nd–Nd clustering, stabilizing *c*-axis growth, and increasing packing density.

At higher temperatures (450–500°C), fast solvent flash-off and short droplet residence time form limited-growth zones, resulting in secondary nucleation, surface disorder, and partial re-evaporation of Nd species. These impacts increase roughness and porosity while marginally decreasing crystallographic order. Annealing at 1000°C alters physical properties by eliminating hydroxyl groups and organic residues, enhancing grain coalescence, and healing oxygen-related flaws. Thermal purification improves refractive index, lowers porosity, and enhances Nd^{3+} radiative efficiency by preventing nonradiative recombination pathways. These mechanisms explain why the 2.97 at.% Nd film deposited at 430°C achieves the best balance of structural compactness, crystallinity, and UC performance.

3.11 | Benchmarking Against State-of-the-Art Up-Conversion Thin Films

To evaluate the performance of the Nd^{3+}:ZnO thin films created in this study, it is necessary to compare their UCQY, excitation wavelength, and manufacturing technique to the most relevant RE-doped oxide thin films and nanostructures described in the literature. Although Er^{3+}/Yb^{3+}-sensitized ZnO systems have produced reasonably high UCQY values under 980 nm excitation, no earlier work has demonstrated visible UC from single-ion Nd^{3+}:ZnO thin films under 808 nm excitation. Table 5 presents key performance data for representative systems and illustrates the benefits of the temperature-controlled AACVD technique presented in this work.

The Nd^{3+}:ZnO thin films generated in this work achieve one of the greatest UCQY values known for single-ion RE-doped oxide thin films under 808 nm excitation, while concurrently benefiting from the scalability and atmospheric-pressure operation of AACVD. Unlike Er^{3+}/Yb^{3+} systems that rely on sensitizer-activator coupling, the present films achieve visible UC by a single-dopant ESA/ET/CET/CR mechanism facilitated by controlled Nd inclusion and tailored microstructures. This benchmarking underlines the significance of the temperature-dependent process-structure-property mapping established in this study. It also emphasizes the technological relevance of Nd-activated ZnO films for photonic and energy conversion applications.

TABLE 5 | Comparison of UCQY, excitation wavelength, and deposition method for representative RE-doped UC thin films and nanostructures.

System	UCQY (%)	Excitation (nm)	Deposition method	Notes/limitations
This work: Nd^{3+}:ZnO thin films	4.25 ± 0.1	808	AACVD (atmospheric pressure)	First visible UC from Nd^{3+}:ZnO films; temperature-controlled incorporation; scalable large-area deposition
ZnO:Er, Yb thin films (AACVD) [14]	5.6	980	AACVD	Requires sensitizer–activator pair; not single-ion UC; different mechanism (CET-dominated)
Nd:Y_2O_3 thin films (AACVD) [12]	~1–2	808	AACVD	Down-conversion dominant; weak visible UC; higher porosity; limited densification
Nd:ZnO nanodisks (CVD) [40–42]	N/A (UC not reported)	808	CVD	Only IR emission (920, 1060 nm); no visible UC; morphology-dependent light trapping
β-$NaYF_4$:Yb, Er (bulk) [5, 6]	−12	980	Solid-state/ hydrothermal	Benchmark UC materials but not thin films; not compatible with Si substrates; not scalable for coatings
ZnO:Er thin films (PLD) [10, 43]	N/A	980	PLD	High quality but expensive; limited area; low UCQY in thin-film form

4 | Conclusion

AACVD was used to produce Nd^{3+}-doped ZnO thin films. The best deposition temperature was 430°C, resulting in dense, highly crystalline, and *c*-axis-oriented films. Post-annealing at 1000°C enhances phase purity and lattice ordering. The optimized film (2.97 at.% Nd) demonstrated robust visible up-conversion at 540, 618, and 680 nm, driven by a two-photon ESA/ET/CET/CR mechanism. It attained a UCQY of 4.25 ± 0.01%, surpassing various benchmark UC materials. Nd concentration affects crystallinity, porosity, refractive index, and UC efficiency, with 2.97 at.% resulting in the best equilibrium. This investigation shows that atmospheric-pressure AACVD can produce cost-effective Nd-activated up-conversion thin films with practical applications in photovoltaics, optical sensors, and photonic devices. These findings demonstrate that Nd^{3+} doping is an effective strategy for engineering ZnO thin films with enhanced densification, reduced nonradiative defects, and optimized optical pathways, ultimately enabling a measurable increase in up-conversion quantum yield. This study establishes a temperature-dependent AACVD mapping framework that links rare-earth incorporation, crystallinity, and densification to UC performance in oxide thin films, supporting both scientific progress and commercially viable large-area manufacturing.

Author Contributions

Ridha Elleuch, **Marwa ben Chobb**, **Jean-Luc Deschanvrese**, **Youssef O. Al-Ghamdi**: conceptualization, methodology, validation, formal analysis, resources, writing – original draft, visualization. **Ikram Benammar**, **Ramzi Maalej**: data curation, visualization. **Abdullah Y. A. Alzahranie**, **Sherif M. A. S. Keshk**: investigation, writing – review & editing, validation, data curation.

Conflicts of Interest

The authors declare that they have no known competing financial interests or personal relationships that could have appeared to influence the work reported in this paper.

Data Availability Statement

Data will be made available on request.

References

1. H. Yan, W. Cao, Z. Wang, Y. Cui, and G. Qian, "Dynamic Manipulation of Upconversion Luminescence by Constructing Metal–organic Framework and Lanthanide-Doped Nanoparticle Composites," *CrystEngComm* (2024): 22–29, https://doi.org/10.1039/D4CE00932K.

2. J. Xu, H. Cao, C. Wu, T. Wang, L. Sun, and B. Dong, "Recent Progress on Rare-Earth-Doped Upconversion Nanomaterials for Bioassay Applications," *Biosensors* (2025): 335, https://doi.org/10.3390/bios15060335.

3. R. Singh, E. Madirov, D. Busko, et al., "Harvesting Sub-Bandgap Photons via Upconversion for Perovskite Solar Cells," *ACS Applied Materials & Interfaces* (2021): 54874–54883, https://doi.org/10.1021/acsami.1c13477.

4. L. Zhao, X. Chen, X. Wang, et al., "One-Step Solvothermal Synthesis of a Carbon@TiO_2 Dyade Structure Effectively Promoting Visible-Light Photocatalysis," *Advanced Materials* (2010): 3317–3321, https://doi.org/10.1002/adma.201000660.

5. Y. Gao, S. Murai, K. Shinozaki, and K. Tanaka, "Up-to-Five-Photon Upconversion from Near-Infrared to Ultraviolet Luminescence Coupled to Aluminum Plasmonic Lattices," *ACS Applied Materials & Interfaces* (2023): 9533–9541, https://doi.org/10.1021/acsami.2c14990.

6. J.-C. Boyer and F. C. J. M. van Veggel, "Absolute Quantum Yield Measurements of Colloidal $NaYF_4$: Er^{3+}, Yb^{3+} Upconverting Nanoparticles," *Nanoscale* (2010): 1417–1419, https://doi.org/10.1039/C0NR00253D.

7. M. Saboktakin, X. Ye, S. J. Oh, et al., "Metal-Enhanced Upconversion Luminescence Tunable through Metal Nanoparticle–Nanophosphor Separation," *ACS Nano* (2012), https://doi.org/10.1021/nn302466r.

8. V. Somjit, P. Thinsoongnoen, S. Waiprasoet, et al., "Processable UiO-66 Metal–Organic Framework Fluid Gel and Electrical Conductivity of Its Nanofilm with Sub-100 nm Thickness," *ACS Applied Materials & Interfaces* (2021), https://doi.org/10.1021/acsami.1c07262.

9. A. Khitous, L. Noel, C. Molinaro, L. Vidal, S. Grée, and O. Soppera, "Sol–Gel TiO_2 Thin Film on Au Nanoparticles for Heterogeneous Plasmonic Photocatalysis," *ACS Applied Materials & Interfaces* (2024): 10856–10866, https://doi.org/10.1021/acsami.3c15866.

10. P. R. Willmott and J. R. Huber, "Pulsed Laser Vaporization and Deposition," *Reviews of Modern Physics* (2000): 315–328, https://doi.org/10.1103/RevModPhys.72.315.

11. X. Hou, and K-L. Choy, "Processing and Applications of Aerosol-Assisted Chemical Vapor Deposition," *Chemical Vapor Deposition* (2006): 583–596, https://doi.org/10.1002/cvde.200600033.

12. R. Elleuch, R. Salhi, J.-L. Deschanvres, and R. Maalej, "Highly Efficient NIR to Visible Upconversion in a ZnO: Er, Yb Thin Film Deposited by a AACVD Atmospheric Pressure Process," *RSC Advances* (2015): 60246–60253, https://doi.org/10.1039/C5RA10442D.

13. K. Imoni-Ogbe, O. M. Osiele, O. V. Akpoveta, et al., "Enhanced Material, Structural, Optical, and Electrical Characterization of Fabricated Aluminium-Doped Zinc Oxide Thin Films Deposited via Aerosol-Assisted-Chemical-Vapor-Deposition (AACVD) Using Oxygen as a Carrier Gas," *Discover Materials* 5 (2025), https://doi.org/10.1007/s43939-025-00284-w.

14. R. Elleuch, M. B. Chobba, J.-L. Deschanvres, et al., "Interfacial Energy Transfer and Charge Separation in rGO/Y_2O_3/ZnO:Er, Yb Plasmonic Hybrid Nanostructures for Photovoltaic Enhancement," *Journal of Alloys and Compounds* (2026): 185641, https://doi.org/10.1016/j.jallcom.2025.185641.

15. E. A. Mikhalyova, O. V. Khomenko, K. S. Gavrilenko, V. P. Dotsenko, A. W. Addison, and V. V. Pavlishchuk, "Absorption- and Excitation-Modulated Luminescence of Pr^{3+}, Nd^{3+}, and Lu^{3+} Compounds with Dianions of Tetrafluoroterephthalic and Camphoric Acids," *ACS Omega* (2019): 2669–2675, https://doi.org/10.1021/acsomega.8b02388.

16. R. Elleuch, R. Salhi, J.-L. Deschanvres, and R. Maalej, "Antireflective Downconversion ZnO: Er^{3+}, Yb^{3+} Thin Film for Si Solar Cell Applications," *Journal of Applied Physics* (2015): 055301, https://doi.org/10.1063/1.4906976.

17. J. L. Pouchou and J. F. Thiot, Procedures for X-Ray Microanalysis of Layered Structures: Accuracy and Limits, *Report Number: CONF-960877* (San Francisco Press, Inc, 1996), https://www.osti.gov/biblio/468846.

18. R. Salhi, H. Roussel, P. Chaudouët, R. Maalej, M. Fourati, and J.-L. Deschanvres, "Effect of Humidity and UV Assistance on the Properties of Erbium Doped Yttrium Oxide Films Prepared by Aerosol-MOCVD," *Chemical Vapor Deposition* (2011): 93–97, https://doi.org/10.1002/cvde.201006877.

19. R. Elleuch, R. Salhi, J.-L. Deschanvres, P. G. Gucciardi, and R. Maalej, "Growth Rate Induced High Efficient Light Trapping/Photon Conversion ZnO: Nd^{3+} Nanodisk Shaped Thin Films Deposited by AACVD Process," *Journal of Alloys and Compounds* (2015): 756–763, https://doi.org/10.1016/j.jallcom.2015.08.157.

20. S. Dhara and P. K. Giri, "Quick Single-Step Mechanosynthesis of ZnO Nanorods and Their Optical Characterization: Milling Time Dependence," *Applied Nanoscience* (2011): 165–171, https://doi.org/10.1007/s13204-011-0026-z.

21. O. İloğlu and H. A. Yurtsever, "The Effects of Annealing Temperature on the Thickness, Morphology, Band Gap Energy, and Photocatalytic Performance of ZIF-8-Derived ZnO/TiO_2 Thin Films," *Journal of Materials Science: Materials in Electronics* (2024), https://doi.org/10.1007/s10854-024-12932-7.

22. L. Qi, Y. Qi, Z. Chai, and Y. Qi, "Post-Annealing Induced Oxygen Vacancy Mediated Non-Polar ZnO Films with Excellent Opto-Electronic Performance," *Ceramics International* (2019): 8388–8394, https://doi.org/10.1016/j.ceramint.2019.01.147.

23. N. Sadananda Kumar, K. V. Bangera, and G. K. Shivakumar, "Effect of Annealing on the Properties of Zinc Oxide Nanofiber Thin Films Grown by Spray Pyrolysis Technique," *Applied Nanoscience* (2014): 209–216, https://doi.org/10.1007/s13204-012-0190-9.

24. A. Abdel-Galil, M. S. A. Hussien, and M. R. Balboul, "Optimal Thickness and Annealing Temperature for Enhancement of Structural, Optical, and Photocatalytic Properties of ZnO Thin Films," *Journal of the Australian Ceramic Society* (2022): 1667–1683, https://doi.org/10.1007/s41779-022-00802-6.

25. A. H. Haritha, M. E. Cruz, O. Sisman, et al., "Influence of Annealing Temperature on the Photocatalytic Efficiency of Sol-Gel Dip-Coated ZnO Thin Films in Methyl Orange Degradation," *Open Ceramics* (2025): 100727, https://doi.org/10.1016/j.oceram.2024.100727.

26. T. Ivanova, A. Harizanova, T. Koutzarova, B. Vertruyen, and R. Closset, "Sol–Gel Synthesis of ZnO: Li Thin Films: Impact of Annealing on Structural and Optical Properties," *Crystals* (2024), https://doi.org/10.3390/cryst14010006.

27. R. Elleuch, R. Salhi, J.-L. Deschanvres, and R. Maalej, "Antireflection and Downconversion Response of Nd^{3+} Doped Y_2O_3/Si Thin Film Deposited by AACVD Process," *Chemical Physics Letters* (2014): 1–7, https://doi.org/10.1016/j.cplett.2014.07.007.

28. B. Poornaprakash, U. Chalapathi, S. V. P. Vattikuti, et al., "Chemical, Morphological, Structural, Optical, and Magnetic Properties of $Zn_{1-x}Nd_xO$ Nanoparticles," *Journal of Materials Science: Materials in Electronics* (2018), https://doi.org/10.1007/s10854-018-0203-x.

29. M. Lal, P. Sharma, and C. Ram, "Optical, Structural Properties and Photocatalytic Potential of Nd-ZnO Nanoparticles Synthesized by Hydrothermal Method," *Results in Optics*. (2023): 100371, https://doi.org/10.1016/j.rio.2023.100371.

30. T. T. T. Huong, N. T. Sa, N. T. M. Thuy, et al., "Eu^{3+}-Doped ZnO Quantum Dots: Structure, Vibration Characteristics, Optical Properties, and Energy Transfer Process," *Nanoscale Advances*. (2025): 909–921, https://doi.org/10.1039/D4NA00858H.

31. A. S. S. Bilal, M. U. A. Khan, N. Banik, et al., "Dual-Doped ZnO Nanocomposites for Superior Photocatalytic Hydrogen Generation," *Journal of Materials Science: Materials in Engineering* (2025): 104, https://doi.org/10.1186/s40712-025-00327-3.

32. Y. Hamid, R. Matarrese, S. Morandi, L. Castoldi, and L. Lietti, "Pd-Doped SSZ-13 for Low-T NOx Adsorption: An Operando FT-IR Spectroscopy Study," *Topics in Catalysis* (2023), https://doi.org/10.1007/s11244-022-01737-9.

33. E. Nowak, M. Szybowicz, P. Sędzicki, et al., "Spectroscopic Study on the Influence of Post-Processing Annealing on ZnO Films Produced with a Sol-Gel Method," *Thin Solid Films* (2024): 140154, https://doi.org/10.1016/j.tsf.2023.140154.

34. A. Ghazy, M. Safdar, M. Lastusaari, H. Savin, and M. Karppinen, "Advances in Upconversion Enhanced Solar Cell Performance," *Solar Energy Materials and Solar Cells* (2021): 111234, https://doi.org/10.1016/j.solmat.2021.111234.

35. N. K. Vijay, P. N. Maya, S. Mukherjee, et al., "Effect of Annealing Temperature on the Structure and Optical Properties of ZnO Thin Films," *Journal of Physics: Condensed Matter* (2023): 135002, https://doi.org/10.1088/1361-648X/ad1361.

36. K. S. Babu, A. R. Reddy, C. Sujatha, and K. V. G. Reddy, "Annealing Effects on Photoluminescence of ZnO Nanoparticles," *Materials Letters* (2013): 10–12, https://doi.org/10.1016/j.matlet.2013.07.114.

37. A. Karmakar, T. Chakraborty, S. Chakravarty, et al., "The Influence of Nd^{3+} Doping on the Structural, Optical, Magnetic, and Dielectric Characteristics of Nanoscale Hexagonal Wurtzite Type ZnO," *Journal of Magnetism and Magnetic Materials* 591 (2024), https://doi.org/10.1016/j.jmmm.2024.171728.

38. P. Pascariu, C. Cojocaru, P. Samoila, and C. Romanitan, "Nd-Doped ZnO Nanostructures with Enhanced Photocatalytic Performance for Environmental Protection," *International Journal of Molecular Sciences* (2023), https://doi.org/10.3390/ijms24076436.

39. I. Iparraguirre, J. Azkargorta, J. M. Fernández-Navarro, M. Al-Saleh, J. Fernández, and R. Balda, "Laser Action and Upconversion of Nd^{3+} in Tellurite Bulk Glass," *Journal of Non-Crystalline Solids* (2007): 990–992, https://doi.org/10.1016/j.jnoncrysol.2006.12.103.

40. N. Tarasenka, V. Kornev, A. Ramanenka, R. Li, and N. Tarasenko, "Photoluminescent Neodymium-Doped ZnO Nanocrystals Prepared by Laser Ablation in Solution for NIR-II Fluorescence Bioimaging," *Heliyon* (2022): e09554, https://doi.org/10.1016/j.heliyon.2022.e09554.

41. B. Yang, J. Cang, Z. Li, and J. Chen, "Nanocrystals as Performance-Boosting Materials for Solar Cells," *Nanoscale Advances* (2024): 1331–1360, https://doi.org/10.1039/D3NA01063E.

42. G. A. Nowsherwan, M. Azhar, N. Anwar, et al., "Exploring the Advanced Optoelectronic Properties of Nd-Doped ZnO Thin Films for Next-Generation Perovskite Solar Cells," *ACS Omega* (2025): 18251–18269, https://doi.org/10.1021/acsomega.4c08108.

43. D. B. Chrisey and G. K. Hubler, *Pulsed Laser Deposition of Thin Films* (John Wiley & Sons, 1994).